




# Development and characterisation of an alginate and expanded graphite based composite for thermochemical heat storage

Jack Reynolds<sup>1,\*</sup> , Rhodri Williams<sup>1</sup>, Jonathon Elvins<sup>1</sup>, Eifion Jewell<sup>1</sup>, Justin Searle<sup>1</sup>, and Xinyuan Ke<sup>2</sup>

<sup>1</sup> Specific IKC, Baglan Bay Innovation Centre, Swansea University, Central Avenue, Port Talbot SA12 7AX, UK

<sup>2</sup> Department of Architecture and Civil Engineering, University of Bath, Claverton Down, Bath BA2 7AY, UK

Received: 22 November 2022

Accepted: 4 March 2023

Published online:  
18 March 2023

© The Author(s) 2023

## ABSTRACT

Thermochemical heat storage is one of the most attractive technologies to store heat from solar thermal energy or waste heat from industrial processes for its high energy density and long-term storage capability. This research presents a novel expanded graphite/alginate polymer matrix encapsulated with hydrated salts as highly efficient thermochemical heat storage materials. Through the simple synthesis method, the composite material can be sized and shaped to fit multiple applications, and be easily scaled where needed. Through the reversible hydration and dehydration reaction, the incorporated  $\text{CaCl}_2$  salt can store and release heat. Thermal energy from solar thermal generators or low grade waste heat sources ( $< 200\text{ }^\circ\text{C}$ ) is appropriate for the dehydration of  $\text{CaCl}_2$ . A salt loading value of 84% has been achieved with visible porosity maintained. Static heat is used to study the charge reaction, whereas a flow of humid air through a packed bed is used to study the discharge reaction where temperature uplifts between  $10\text{--}14\text{ }^\circ\text{C}$  were observed. A vermiculite/ $\text{CaCl}_2$  composite is used as a comparison in both reactions. Additionally, bulk density, surface porosity, surface area, moisture sorption and thermal conductivity are considered. The results show that the novel composite materials developed in this study can achieve better packing density and comparable energy density comparing to the conventional vermiculite/ $\text{CaCl}_2$  composite, but with higher thermal conductivity leading to enhanced energy efficiency.

Handling Editor: Chris Cornelius.

Address correspondence to E-mail: 865797@swansea.ac.uk

E-mail Addresses: Rhodri.J.Williams@Swansea.ac.uk; Jonathon.Elvins@Swansea.ac.uk; E.Jewell@Swansea.ac.uk; J.R.Searle@Swansea.ac.uk; xk221@bath.ac.uk

## GRAPHICAL ABSTRACT



## Introduction

Due to the depletion of the world's fossil fuel reserves and the deterioration of the environment in modern times, it is imperative to change the way energy is produced, stored, and used. Almost 50% of the energy consumed in the UK (760 TWh) was needed for heating applications in 2017, of which domestic space heating accounted for 57% [1]. Only 4.5% of the energy used to heat the UK's 29 million homes and non-residential building was from a low carbon energy source. This value needs to significantly increase if the UK is to meet its carbon zero target for 2050 [2, 3]. Solar heat and industrial waste heat (IWH) are two low carbon sources associated with an abundance of heat energy, however there are problems that are linked to both sources where generation and utilisation often do not align. There is a timing mismatch (diurnally and seasonally) for solar heat, whereas for IWH there is a location mismatch, with the additional problem of discontinuous heat. Effective heat storage in a mobile medium is the solution to both these problems.

Thermochemical heat storage (THS) provides a suitable way to overcome these mismatch issues by utilising a reversible endothermic reaction to store

heat energy. In comparison to sensible heat storage (SHS) and latent heat storage (LHS), THS generally has superior theoretical energy density and the ability to store heat indefinitely, which the other two cannot [4]. Both mobile THS, which transports IWH to an off-site heat application, and inter-seasonal heat storage at the demand location have utilised sorption heat storage technologies [5, 6]. "Salt in Matrix," or SIM, is one of the most widely used sorption THS material in the literature [7–9]. Here, the enthalpy of the reversible hydration reaction of the salt is used to store energy within a physical scaffolding. In addition to providing a large surface area and high porosity to support the sorption kinetics, the matrix also serves as a protective structure to prevent deliquescence-related issues like salt leakage [10]. Vermiculite [11], silica gel [12], activated alumina [13], activated carbon [14] and expanded graphite [15] are typical materials used for this matrix. The latter is used for its low cost and density, large surface area and associated higher thermal conductivity. Although the outcomes look promising, lower bulk densities, agglomeration, and salt leakage mean that expectations for the energy density and cycle stability of the composite are rarely met. [16]. Recently, hybrid salt/expanded graphite pellets were made by adding an organic polyelectrolyte binder [15] and ethyl

cellulose [17] to alleviate some of these issues. Both studies showed improvements in cycle stability in the presence of these additives due to the reduced leakage of salt and even a positive contribution to reaction kinetics. However, compressing expanded graphite into pellets would reduce its internal porosity, making it difficult for reacting air to pass through the composite. Using expanded graphite and nanocellulose, a freeze-drying method was used to create a porous structure to house strontium bromide [18]. When compared to the stand-alone salt hydrate, hydration kinetics were found to improve by 54% due to the structure's high porosity. More recently there has been studies involving the use of sodium alginic acid as a host matrix due to its excellent microscopic shaping properties [19, 20]. Crosslinking (gelation) in the polymer occurs when two  $\text{Na}^+$  cations, which are already present, are displaced in the presence of a divalent cation like  $\text{Ca}^{2+}$  or  $\text{Sr}^{2+}$ . A stable hydrogel is created when the divalent cations coordinate with oxygen atoms from different polymer chains. With this procedure it is possible to make consistent spherical beads. High loading of thermochemically active salts within the matrix has been achieved with storage densities upwards of  $417 \text{ kWh/m}^3$  [20]. In contrast to the more usual matrices, this alginate-derived matrix is a passive host with no micro or mesoporosity.

In this work, a novel approach to combine an alginate polymer, for its ability to be shaped by gelation, with expanded graphite, for its high surface area and thermal conductivity, is considered to achieve a highly porous structure to hold thermochemically active salts. To best of our knowledge this is the first time that these two materials have been successfully combined and used as a matrix for THS applications.  $\text{CaCl}_2$  has been chosen as the incorporated salt because it is both a "gelation salt" and a well-documented and understood thermally active material. It is low cost, has good stability for low and higher temperature charging, and has superior storage properties compared to other salts [17, 21].

## Materials and methods

### Materials

Anhydrous calcium chloride was purchased from Sigma-Aldrich® and the saturated solution was

prepared at room temperature. Sodium alginate was purchased from Sigma-Aldrich® in powder form. Milled expanded graphite (mEG), commercial grade TIMREX® C-THERM012, with  $25 \text{ m}^2/\text{g}$  surface area (as reported in the material data sheet) was purchased from Imerys Graphite & Carbon (Bironico, Switzerland). Expandable graphite grade BLG300L-LT was purchased from RMC Reason GmbH (Bad Säckingen, Germany). This has an expansion start temperature of  $140\text{--}160 \text{ }^\circ\text{C}$ . To obtain expanded graphite (EG), flake samples were heated at  $> 200 \text{ }^\circ\text{C}$  for 1 h.

### Composite synthesis

Figure 1 highlights two different synthesis procedures. Both start with an alginate solution made using a ratio of 1 g of alginate to 50 ml of deionised water. The solution is stirred at elevated temperatures until alginate is fully dissolved. The graphite is then added at the chosen EG:Alg ratio (3:1 or 6:1). The drop-cast method (1) requires immediate dropping of EG/Alg solution into a saturated  $\text{CaCl}_2$  bath. Gelation occurs due to the cross-linkage between  $\text{Ca}^{2+}$  ions and the alginate polymer. Formed beads are soaked in the same solution for  $> 24 \text{ h}$ , allowing diffusion of salt into the matrix. Beads are filtered and dried at  $120 \text{ }^\circ\text{C}$  for a further 24 h. For the mould method (2), the EG/Alg solution is transferred to a mould for freezing, giving more control over the size and shape. To ensure that the beads fully solidify, this is kept at  $-20 \text{ }^\circ\text{C}$  for  $> 2 \text{ h}$ . After that, they are transferred to the saturated  $\text{CaCl}_2$  solution for cross-linking and impregnation over a 24-h period. Again, beads are filtered and dried at  $120 \text{ }^\circ\text{C}$  for 24 h. Table 1 details the beads produced by both methods. An EG-D sample was not considered as the expanded graphite would not form a uniform mixture at the chosen EG:Alg ratio (3:1) which is appropriate for drop-casting.

The visible structure of the beads is completely different depending on which expanded graphite (mEG or EG) is used in SIM synthesis (Fig. 2). The size of the bead is dictated by the method of synthesis. Method 1 creates beads in the range of 3–4 mm whereas a 6 mm spherical mould is used to synthesize the beads for Method 2. According to Kallenburger et al., the concentration of the alginate solution, the concentration of the gelation salt solution, and the size of the droplet can control the size of

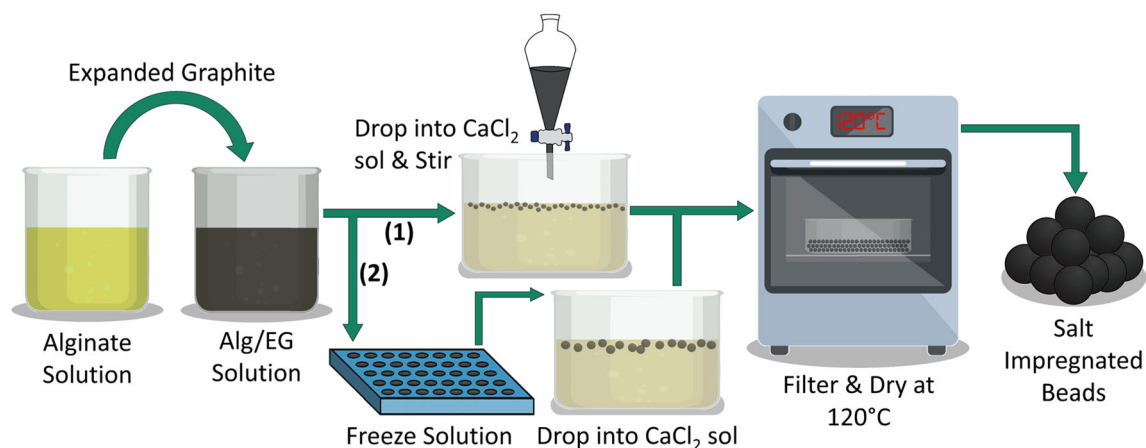


**Figure 1** Schematic illustration of fabrication of  $\text{CaCl}_2$  impregnated EG/Alg beads. (1) Drop-cast method. (2) Mould method.

**Table 1** Summary of synthesized composites

Sample	Method	Size (mm)	Expanded graphite	EG:Alg
mEG-D	Drop cast	3–4	C-Therm012	3:1
mEG-M	Mould	6	C-Therm012	6:1
EG-M	Mould	6	BLG300-LT	6:1
V- $\text{CaCl}_2$	Incipient wetness	2–7	–	–

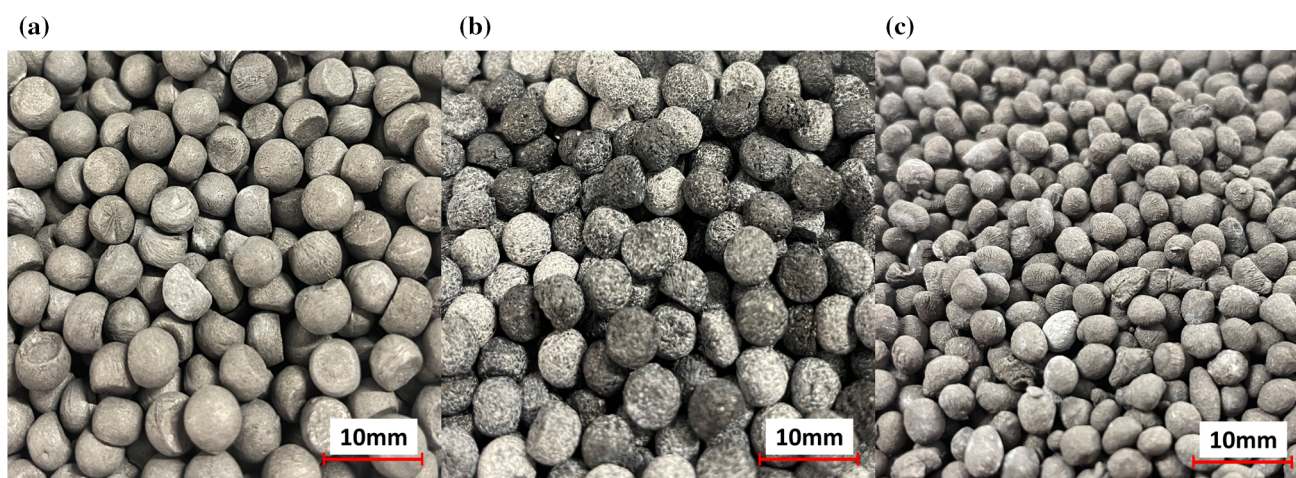


**Figure 2** Optical Images of EG/Alg composites. **a** mEG-M, **b** EG-M, **c** mEG-D.

the beads, which can range from 0.5 to 5 mm [20]. The packing density, bulk density, and flow of reacting air are affected by the size of the formed beads. In a packed bed, smaller beads will increase the bulk density but restrict air flow through the material. The concentration of  $\text{CaCl}_2$  in the gelation bath can be used to regulate salt loading. For this study, only a concentrated solution is considered (74.5 g/100 mL). These parameters will control the performance of the SIM during the charge and

discharge cycles and the optimum synthesis parameters are to be found.

### Experimental procedures

To examine the internal morphology of the composite beads a Zeiss Evo LS25 scanning electron microscope (SEM) with a 15 kV accelerating voltage was used. Further to this electron dispersive spectroscopy (EDS) was utilised to validate that the salt was fully penetrated to the centre of the bead's structure. Beads

were sliced to make semi spherical structures with a flat plane through the centre. Titration analysis of the chloride ion concentration (Mohr's Method) was used to determine the salt loading of the composites. The composite (3 g) is washed in DI water (100 ml) for > 1 h dissolving all the  $\text{CaCl}_2$  that is present. A potassium chromate indicator is used to titrate this solution against a silver nitrate solution. The  $\text{AgNO}_3$  preferentially reacts with chloride ions in solution to form a precipitate of  $\text{AgCl}$ . A colour change from yellow to orange then indicates the formation of silver chromate due to the complete consumption of the chloride ion. Determination of the chloride ion concentration from the titration volume then enables the calculation of the  $\text{CaCl}_2$  present in the sample. The bulk density of the sample was calculated from their mass reading (measured on a Ohaus Scout STX223 with a readability of 0.001 g) in a known volume of a cylindrical container. The volume of the container is calculated from the filled mass of water ( $1 \text{ g} = 1 \text{ cm}^3$ ). A Keyence VHX-7000 digital microscope was used to examine the surface porosity of the resulting composites. The 3D scanning mode combined with spherical shape correction allows for a flat topographic image to be produced. The volume measurement option can then be used to highlight specific areas based on their z-axis position. The keyence microscope was also used to calculate the size distribution of the expanded graphite samples. The Micrometrics Tristar II 3020 is used to calculate the surface area of the porous structures by utilising the isotherm of  $\text{N}_2$  physisorption and the multipoint Brunauer–Emmett–Teller (BET) method. Prior to analysis, using a micrometric VapPrep 061, samples were dried and degassed with nitrogen at  $120 \text{ }^\circ\text{C}$  for > 12 h. Thermogravimetric analysis (TGA) and static charge analysis (SCA) was conducted at large scale (5 g) using the Ohaus MB120. The samples were exposed to a relative humidity (RH) of 20% and a temperature of  $30 \text{ }^\circ\text{C}$  for more than 168 h to attain a consistent hexahydrate state. For TGA, 5 g of sample was subject to a temperature ramp of  $1 \text{ }^\circ\text{C}/\text{min}$  from 20 to  $200 \text{ }^\circ\text{C}$ . For SCA, 5 g of each sample were subject to three different drying temperatures ( $120 \text{ }^\circ\text{C}$ ,  $150 \text{ }^\circ\text{C}$  &  $200 \text{ }^\circ\text{C}$ ). A custom-built assembly is used to measure the composites' discharge performance (Fig. 3). Materials are dried for > 24 h at  $120 \text{ }^\circ\text{C}$  prior to testing to guarantee the anhydrous state.

A Cellkraft P-50 RH generator is used to produce moist air which is fed into a reactor containing a

predetermined volume of material. A set of three thermocouples are used to measure temperature uplift and bulk temperature. Three load cells at the reactor's base are used to make in situ mass recordings. Thermal conductivity is important to measure the materials capacity of heat transmission. A hot disk thermal constant analyzer (TPS-1000, Hot Disk Inc., Sweden) is used to measure the thermophysical properties of the synthesized composites. Samples are crushed to a powder and dried to an anhydrous state at  $120^\circ\text{C}$ . Each material was loaded into the powder sample holder and subject to 4.4 N. The thermal conductivity ( $k$ ), thermal diffusivity ( $\alpha$ ), and specific heat ( $c_p$ ) of the powder can be accurately measured based on the transient plane heat source method. Dynamic vapor sorption (DVS) was conducted using the DVS Advantage instrument (Surface Measurement Systems) to assess the water sorption kinetics of the composite beads within the RH range of 0–95% at  $25 \text{ }^\circ\text{C}$ . Each test used one bead which was stabilized at 0% RH before conducting the water adsorption isotherm. For Static Vapor Sorption (SVS) tests, materials are dried at  $120 \text{ }^\circ\text{C}$  for >24 h to ensure the anhydrous state is achieved. A Memmert constant climate chamber HPP110eco is used to evenly add moisture to the materials. 3 petri dishes, each containing 10 g of material, were subject to the three chosen RH conditions (25%, 50% and 75% RH at  $25 \text{ }^\circ\text{C}$ ) and left for 168 h to assess the maximum water uptake. Mass recordings were taken every 24 h.

## Results and discussion

### Morphological analysis

SEM was used to look into the bead composites' morphology. The micrographs that highlight the internal structures of the beads are shown in Fig. 4. The samples prepared with mEG clearly show the formation of beads with smaller pores and a large network of graphite scaffolding. This is also highlighted in the 3D surface topography maps (Fig. 5) that are created using the Keyence microscope. The colour scales used are for a depth comparison on the surface of each sample and not for a comparison between samples. Using mEG, beads are produced containing surface pores with a diameter in the range of 20–40  $\mu\text{m}$ , while using the EG a pore size between

**Figure 3** Schematic of the experimental apparatus developed to investigate the discharge performance of typical thermochemical material.

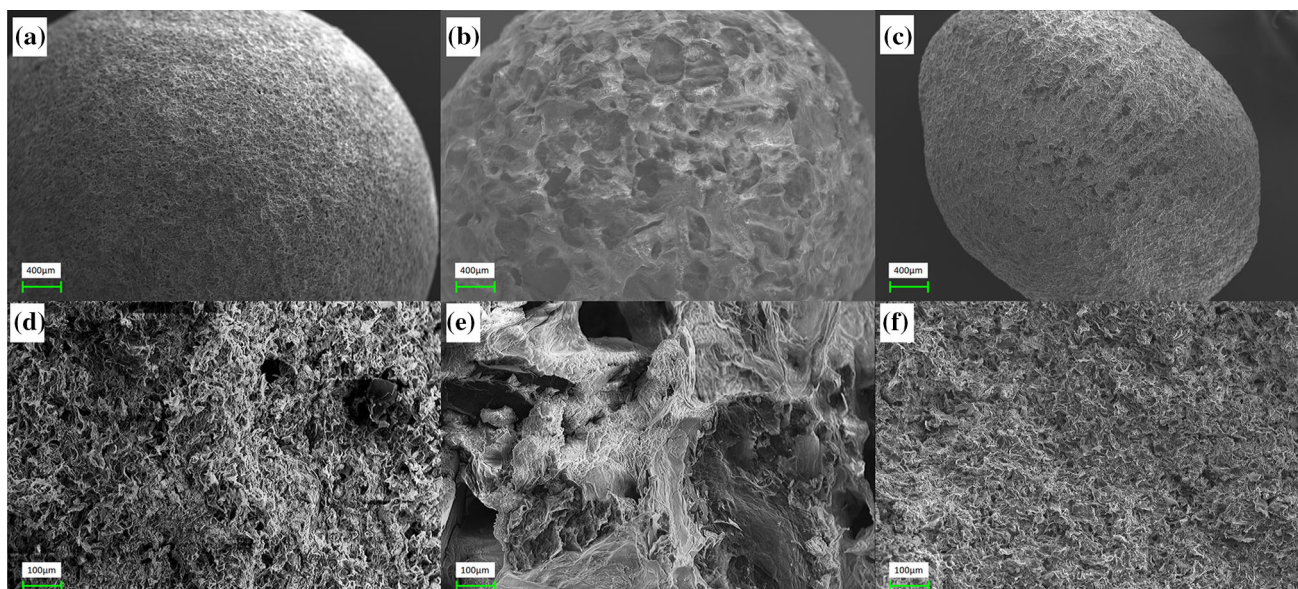
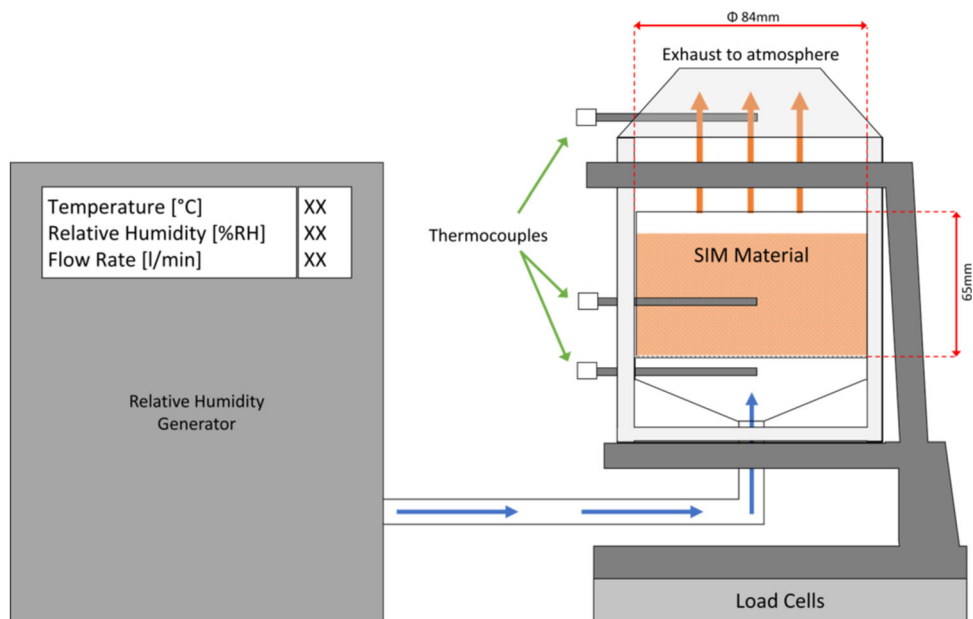


**Figure 4** SEM images showing the surface and internal structures of mEG-M (a, d), EG-M (b, e) and mEG-D (c, f) beads. a-c show surface structure. d-f show the bead cross-section.

100–150 µm is achieved. No substantial difference between the surface structure of mEG-D and mEG-M is observed indicating that this is a direct effect of graphite used. The internal composition of the beads is shown in Fig. 4d,e,f. The EG sample shows both large structures and pores which will allow for good passage of moisture, though the resulting larger CaCl<sub>2</sub> deposits on these structures will reduce the area that is available to a carrier gas. The internal structure of the mEG beads is much finer leading to

smaller deposits of CaCl<sub>2</sub> crystals which is advantageous as it enhances the contact area between a carrier gas and the salt. However, the smaller network of pores may prevent addition/removal of moisture, resulting in slower reaction kinetics. Although the BET method is considered inaccurate for macro-porous materials like vermiculite, it has been used as a comparison between composites considered for THS [7, 22]. The surface area results are shown in Table 2.

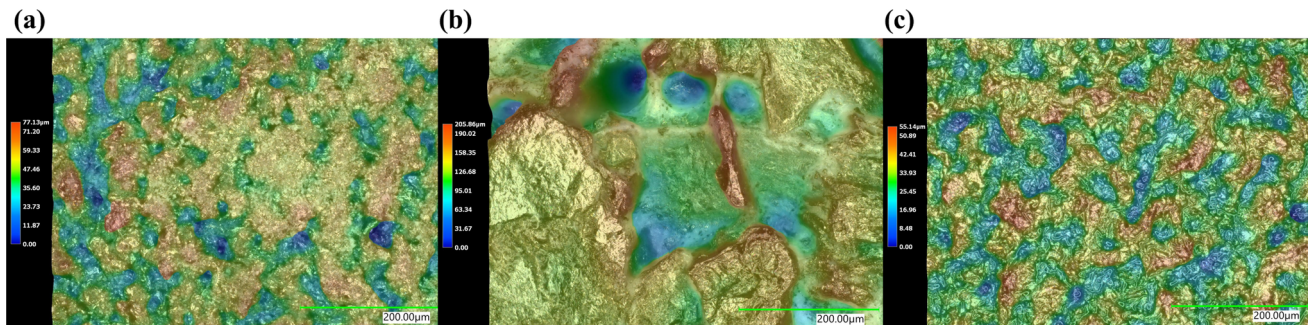


**Figure 5** 3D Surface topography of bead composites at  $\times 300$  magnification. (a) mEG-M, (b) EG-M, (c) mEG-D.

**Table 2** Physical characteristics of the synthesized materials

Sample	Salt loading (%)	Bulk density ( $\text{g}/\text{cm}^3$ )	Salt volumetric density ( $\text{g}/\text{cm}^3$ )	Theoretical storage density ( $\text{MJ}/\text{m}^3$ )	Surface area ( $\text{m}^2/\text{g}$ )	Pore surface area ( $\mu\text{m}^2$ )	Diameter (mm)
mEG-D	78	0.78	0.61	490	4.02	20–40	$3.6 \pm 0.6$
mEG-M	84	0.55	0.46	370	4.49	20–40	$6.1 \pm 0.4$
EG-M	72	0.37	0.26	210	2.80	100–130	$6.3 \pm 0.2$
V- CaCl <sub>2</sub>	70	0.26	0.18	150	1.59	–	2–7

The surface area of all graphite/alginate-based composites is greater than that of the V-CaCl<sub>2</sub> sample. The two mEG samples have the greatest surface area, which would be attributed to the high surface area of the mEG providing a larger space for the salt to crystallize. This indicates that these materials all form smaller crystal structures in their highly porous scaffolding. Of these two samples the moulded beads show a higher surface area. This could be because of the larger mEG:Alginate ratio allowing more space for the salt to crystallise on the graphite surface. Alternatively, this could also be attributed to the freezing nature incorporated into the mould method. The freezing of solution may allow ice crystals to expand the network of pores. Solidification of the scaffolding before the melting then maintains a larger network of pores. Table 2 displays the bead diameter calculated from 30 samples of each expanded graphite material. Due to the less controllable size of the droplets, the beads made using the drop-cast method produce the largest distribution of bead diameter. The bead diameter of the mould method is slightly larger than the mould used (6 mm) showing size is maintained during the gelation stage. The reduced

size distribution over the drop-cast method implies a more uniform packing will be observed. The bulk density tests are shown in Table 2. Compared to V-CaCl<sub>2</sub>, the expanded graphite beads in this study have a higher bulk density. The mEG-D beads have the highest bulk density of the three samples at  $0.78 \text{ g}/\text{cm}^3$ , whereas the mEG-M and EG-M are  $0.55 \text{ g}/\text{cm}^3$  and  $0.37 \text{ g}/\text{cm}^3$  respectively. This is because of their smaller diameter and wider size distribution, which enables them to fill more of the void fraction in a given space. This could be beneficial to obtain more salt per unit of volume, however, the resulting restriction of the carrier gas may have a negative impact on material performance. Of the two mould samples, the mEG samples have a larger bulk density probably due to the larger network of pores allowing more salt to be incorporated.

### Salt characterisation

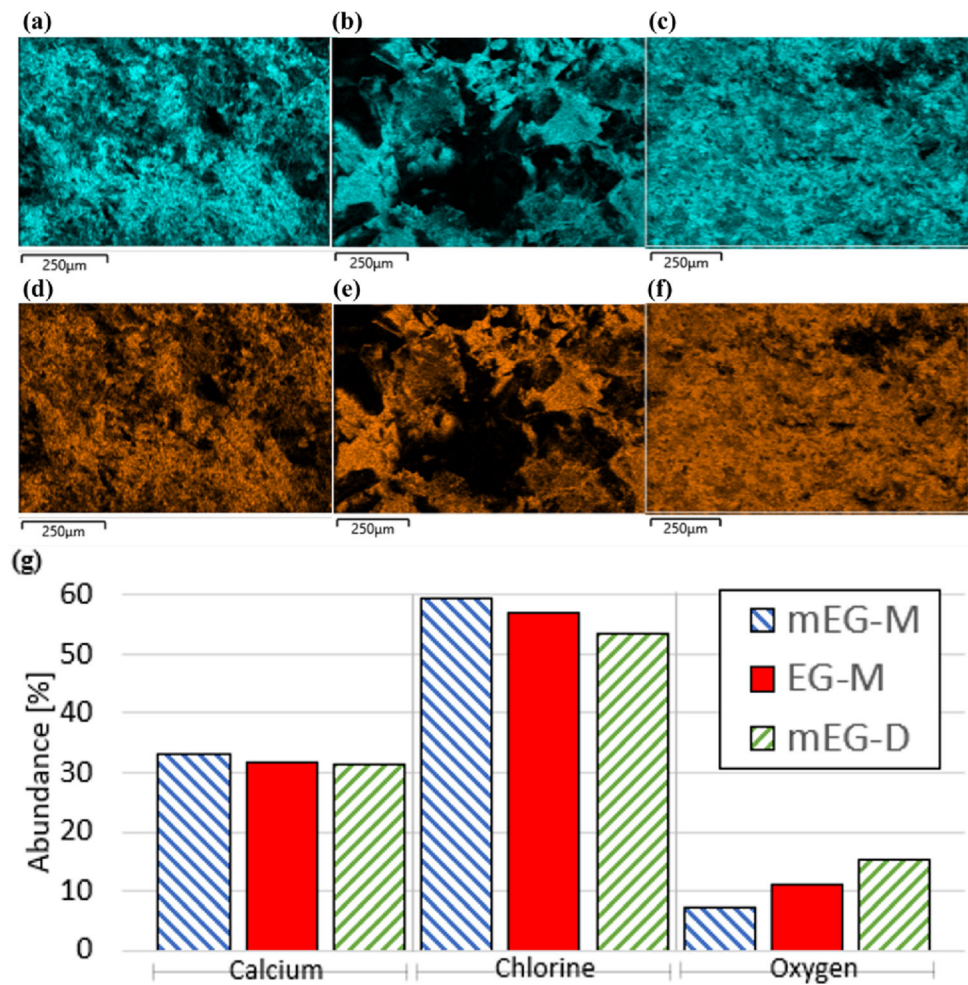
Results from the Mohr's titration indicate the salt loading values for the expanded graphite materials are all higher than the V-CaCl<sub>2</sub> samples when salt content is based on the anhydrous state (Table 2). The

composites can still achieve the high salt loading levels observed with a pure alginate matrix even with the addition of graphite [20]. An estimation of the salt volumetric density is achieved by combining the bulk density values and the salt wt%. The theoretical storage density ( $1.47 \text{ GJ/m}^3$ ) and the powder density ( $1830 \text{ kg/m}^3$ ) for the  $\text{CaCl}_2$  anhydrous state are known from the work done by Barreneche et al. [23]. The maximum theoretical storage density is calculated by combining these numbers with the salt volumetric density of the synthesised materials. The results indicate that mEG-D and mEG-M have approximately 3.5 and 2.5 times more energy storage capacity than V- $\text{CaCl}_2$ .

EDS Analysis of the cross-section of the beads shows the salt solution has been fully absorbed into the centre of the bead structure (Fig. 6). The EDS maps show the mEG samples have a more homogeneous spread of the salt over the matrix scaffolding.

This is expected as the BET surface area of these samples is larger than the corresponding EG samples. The EG samples show uniform layers of salt that have formed on the large EG/Alg structures. This implies that the kinetics of dehydration will be slower as a thicker layer of salt will restrict the loss of water from deeper layers of salt. The EDS spectra all show an approximate 2:1 ratio between Cl and Ca confirming the presence of  $\text{CaCl}_2$ . What is noticeable is that all the Ca wt% values are slightly higher than a 2:1 value which indicates the extra Ca ions contributing to the alginate scaffolding. Of the three samples, the mEG-D has the lowest Ca and Cl wt% which suggests there is a larger amount of scaffolding material (EG/Alg) in comparison to the salt. The higher % of oxygen, lower surface area than mEG-M and the more condensed structure all support this.

**Figure 6** EDS maps of the at the centre of each composite cross-section (a–f). mEG-M (a, d), EG-M (b, e), and mEG-D (c, f). Cl K $\alpha$ 1 signal is highlighted in cyan. Ca K $\alpha$ 1 signal is highlighted in orange. EDS elemental abundance (g).





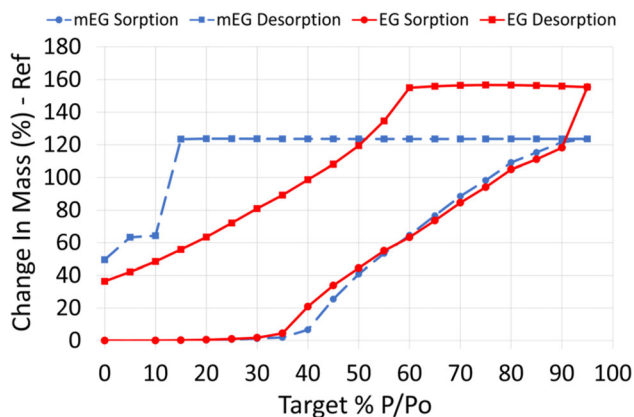


**Figure 7** DVS Isotherm of samples mEG-M and EG-M.

### Water sorption

Figure 7 shows the DVS isotherm obtained from the mEG-M and EG-M samples. Both samples begin to uptake water from around 30–35% RH before following a parallel trend up to the mass increase of 120 wt% at 90% RH. This suggests the  $\text{CaCl}_2$  has reached a level of moisture uptake beyond that of the maximum hydrated state. The materials begin to behave differently as the RH approaches 95%. While the mEG-M sample plateaus, the EG-M sample continues to increase to a gain of 160 wt%. This suggests that deliquescence can occur throughout the EG samples due to the larger pores, whereas deliquescence may be limited by the smaller pores on the surface of mEG. For the desorption cycle, the EG sample begins to lose water at 60% RH, whereas the mEG sample does not begin to lose water until the RH falls below 15%. There are numerous reasons of the observed hysteresis. First, hysteresis is to be expected because the water is bound by chemisorption, so removing this chemically bound water would require more energy. Additionally, the significant desorption hysteresis observed from both samples is most likely due to the existence of ink-bottle-type pore structures [24], consistent with the results depicted in the surface topography and SEM images. The findings indicate that the material with the largest pores desorbed water more easily, suggesting the kinetics of the charge reaction will be faster in the EG samples.

Figure 8 depicts the raw SVS results. All experiments were carried out at 25 °C. The RH values selected were 25%, 50% and 75%. All four materials absorb moisture at a similar rate over the course of 24 h. This is because unreacted salt is more accessible

being closer to or directly on the surface of the aggregates during this time. As the unreacted salt decreases and the reaction approaches equilibrium, the rate of uptake gradually decreases. Beyond 24 h, either the quantity of salt available or the kinetics of moisture transport through the materials differentiate the uptake rate. For the lower RH%, the mEG-D and vermiculite samples show greater water uptake. This is because the salt is more easily accessible in both cases. The bead diameter for mEG-D is much smaller than that of the mould method, therefore reducing the distance required for moisture transport, and the vermiculite salt content is distributed over a larger area. The known salt wt% values and the shape of the mEG-M and EG-M curves at this RH suggest that these samples have not completed water uptake after seven days. After 24 h, the amount of salt dominates the performance of the materials for the 50% and 75% conditions. The raised humidity increases the kinetics of moisture transport to the centre of the larger beads preventing the lag in uptake shown at 25% RH. Looking at moisture uptake per unit volume, considering the bulk density, it is seen that all EG/Alg materials uptake more water than V- $\text{CaCl}_2$  on both the 24 h and 7-days timeframe (Figure 9). Despite having a lower salt volumetric density, the mEG-M performs better than the mEG-D. This suggests that more salt is accessible in the moulded sample due to the larger network of internal pores.

### Thermal properties

Each material was placed inside the vertical, cylinder-shaped reactor with air entering at the base to assess the thermal response (Fig. 3). The reactor was filled with 200  $\text{cm}^3$  of material for each experiment. Using a Cellkraft P-50 RH generator, a flow of air with consistent and controllable parameters is produced. The chosen parameters for the experiments were 25 °C, 60% RH, 20 l/min, for a period of 3 h. The response of each material to the given conditions are depicted in Fig. 10. When exposed to moisture in the air flow, all four materials successfully release the chemically stored heat energy. The temperature profiles here are similar to those of previous studies that used V- $\text{CaCl}_2$ , with an initial temperature spike followed by a gradual temperature decrease [11, 21]. By maintaining a RH of 60% as opposed to > 90%, the water delivery is reduced, resulting in lower maximum temperatures than those observed in

**Figure 8** SVS Analysis of all four samples at 25% (1), 50% (2) & 75% (3) RH.

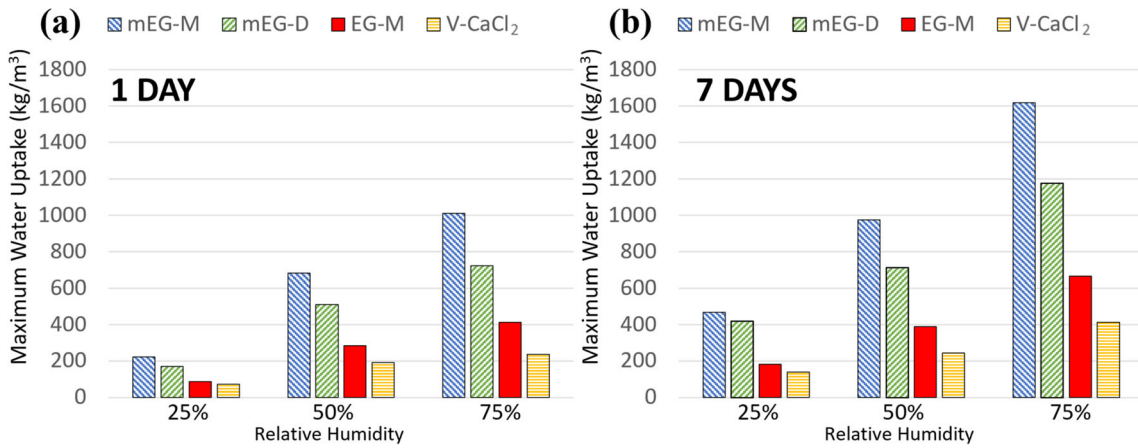
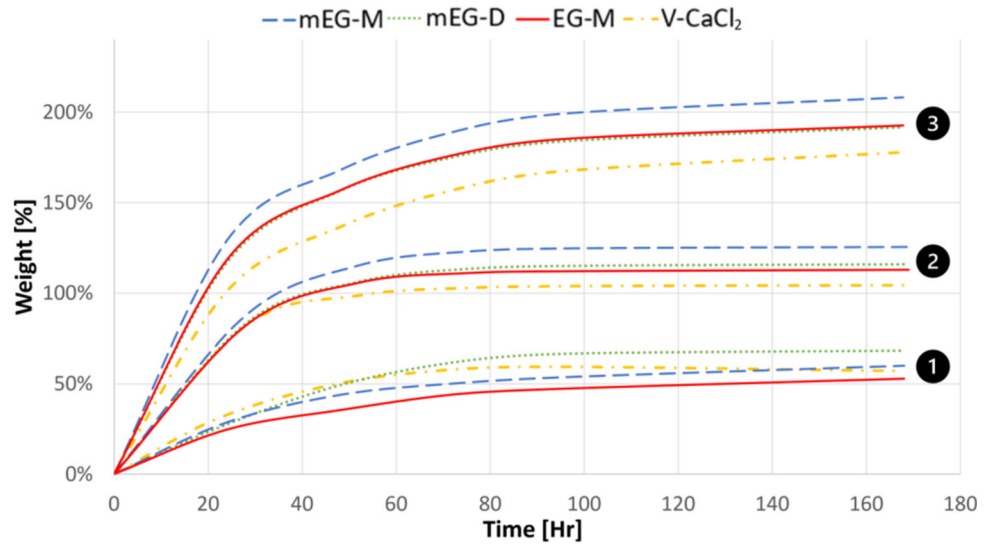
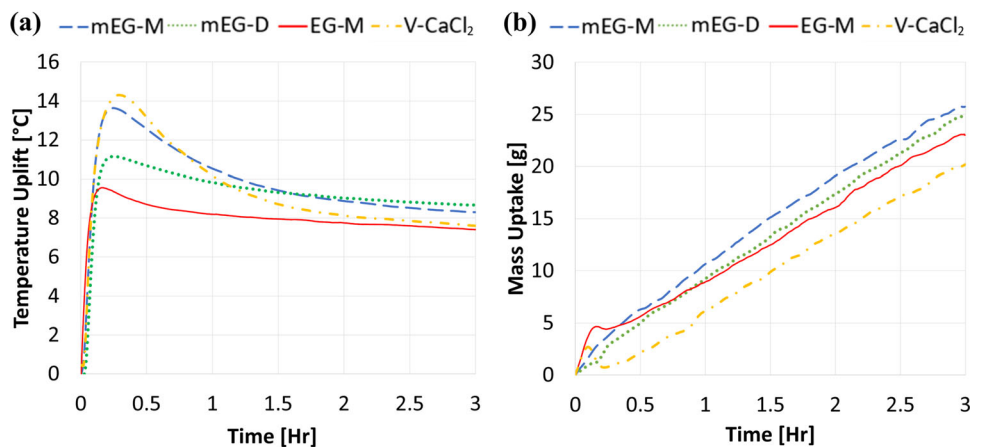


**Figure 9** Water uptake per volume of material over 1 day (a) and 7 days (b).

**Figure 10** Discharge results for each material. Temperature uplift from inlet to outlet (a). Moisture uptake (b).



previous studies. All of the materials behave very similarly, despite the fact that the initial peak temperature varies slightly between samples. This is due

to the fact that the flow of air only delivers a certain amount of moisture. The mass results shows that all four materials uptake moisture at the same rate

( $\sim 7$  g/h) due to the equivalent amount of  $\text{CaCl}_2$  being accessible for absorption over the 3-h cycle. Given that, it is anticipated that the energy output will be comparable. The initial rise in temperature of V- $\text{CaCl}_2$  would indicate that there is a greater amount of salt accessible that is evenly distributed over the larger matrix volume. For the mEG-M sample, it is thought that there is good air flow through the packed bed because of the uniform spherical units. This suggested that the mEG-D peak was lower because the tighter packing caused by the smaller beads prevented sufficient air flow. Instead of a higher observed initial heat release at the outlet, thermal transfer will heat the reactor's localised walls more favorably. Due to its lower salt content, smaller surface area, and harder-to-reach internal salt, the EG-M sample has the lowest peak temperature. Over time, the temperatures of all four materials begin to fall to a lower or plateaued uplift. This is to be expected as less anhydrous  $\text{CaCl}_2$  becomes available over time, less heat will be generated. In addition, the reacting moisture will now have to travel to harder-to-reach locations, reducing the kinetics of moisture uptake thus gradually decreasing the temperature uplift. Even so, after three hours, the EG/Alg materials continue to exhibit good uplift and show no obvious signs of reduction. A comparison of the moisture uptake value to the theoretical mass uptake to achieve a uniform hexahydrate state is used to comprehend the state of discharge. Table 3 highlights the amount of  $\text{CaCl}_2$  available for each experiment and the amount of water needed to reach the maximum hydrated state. A presumption that all materials have absorbed 25 g of water is used to calculate the reaction percentage. Results show that all EG/Alg materials have far more energy to release than V- $\text{CaCl}_2$ . The TGA of fully hydrated materials on a large scale (5 g at  $1^\circ\text{C}/\text{min}$ ) is depicted in Fig. 11. The dehydration behaviour of the EG/Alg composites are almost identical to that of V- $\text{CaCl}_2$ , with the

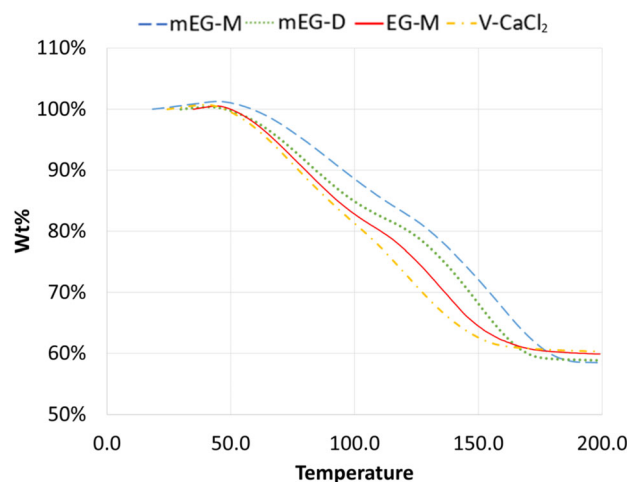


**Figure 11** Thermal gravimetric analysis (TGA) of 5 g of materials conducted on the Ohaus MB120 at  $1^\circ\text{C}/\text{min}$ .

exception of slightly slower rates of dehydration at each significant step. This is because the salt volumetric densities are higher and there is more salt per mass of material. Under these heating conditions two weight loss steps are observed. The first one is ascribed to the transition from hexahydrate to a region typical of a mixture of tetrahydrate and dihydrate ( $\sim 80$  wt%). If the heating rate were slower, a third transition between these states would likely be visible, as shown by previous studies [25]. The second weight loss step is visible for all four materials which is related to the complete dehydration to anhydrous salt ( $< 60$  wt%). This final step occurs at different temperatures for each of the materials, possibly due to a decrease in dehydration kinetics that causes a lag in the transition temperature for the graphite-based materials. The slower charge kinetics observed in the mEG-M sample, compared to the EG-M sample, are consistent with the DVS results. Based on these results, it is possible that all four materials can be fully dehydrated at  $120^\circ\text{C}$ . Figure 12 shows static dehydration conducted at  $120^\circ\text{C}$ ,  $150^\circ\text{C}$ , and  $200^\circ\text{C}$ . Mass data is recorded

**Table 3** Estimation of reaction progression of each material based on the mass of  $\text{CaCl}_2$  and water uptake

Sample	Volume of material ( $\text{cm}^3$ )	Mass of $\text{CaCl}_2$ (g)	Hexahydrate mass uptake (g)	Reaction %
mEG-D	200	121.2	118.0	21
mEG-M	200	91.8	89.4	28
EG-M	200	52.6	51.2	49
V- $\text{CaCl}_2$	200	34.8	33.9	74

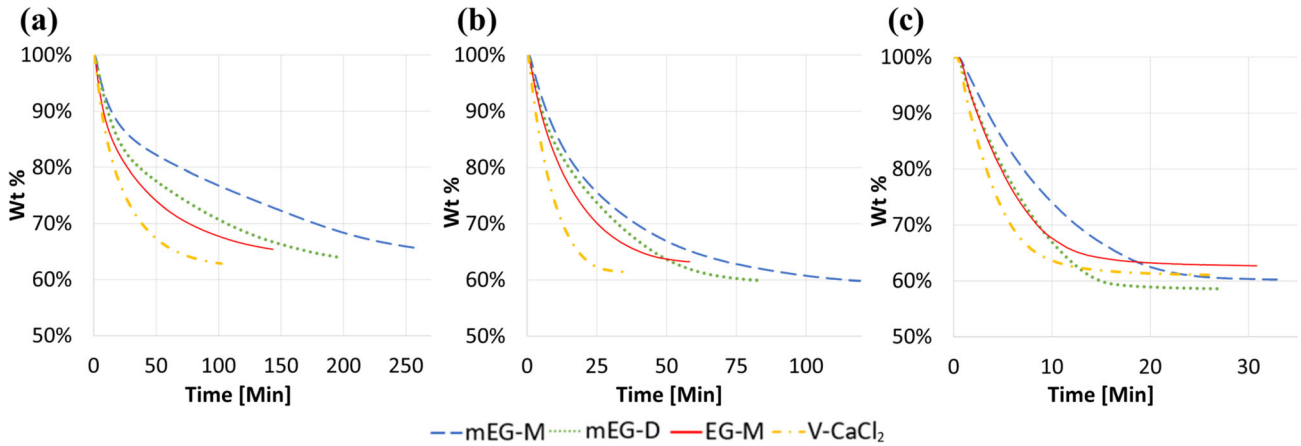


**Figure 12** Static Drying of 5 g of material in the Ohaus MB120 at 120 °C (a), 150 °C (b), and 200 °C (c).

until a variation of less than + / – 1 mg change is seen over 120 s. Like the results shown in the TGA analysis, a higher rate of dehydration in all three instances is observed for V-CaCl<sub>2</sub> as salt is distributed over a significantly larger volume. Of the three expanded graphite materials, mEG-M shows the slowest rate. This is because it has a smaller structural porosity than EG-M and a larger spherical shape than mEG-D (larger distance for moisture transport). Again, this is in line with the desorption curves from the DVS analysis.

Thermal Analysis was conducted on the powder samples of materials under consideration and their substituents Fig. 13. Thermal conductivity (*k*) of a material is a measure of the ability of that materials to conduct heat through it, whereas thermal diffusivity ( $\alpha$ ) can be understood as the ability to conduct heat

relative to the heat stored per unit volume, or specific heat capacity (*c<sub>p</sub>*). The relationship between the three is shown in Eq. 1:

$$k = \alpha c_p \tag{1}$$

For the base materials, the expanded graphite has a far higher thermal conductivity in powder form than vermiculite. Of the two, BLG has superior thermal conductivity possibly because of the better interconnections between graphite layers than the pure milled form (C-Therm012). However, when looking at the composite materials the same trend is not shown. mEG-M has the highest conductivity followed by EG-M and then V-CaCl<sub>2</sub>. This could be because the synthesis process has broken down the lamella structures of BLG or the larger air gaps still present in its powder form. mEG-M has maintained 66% of

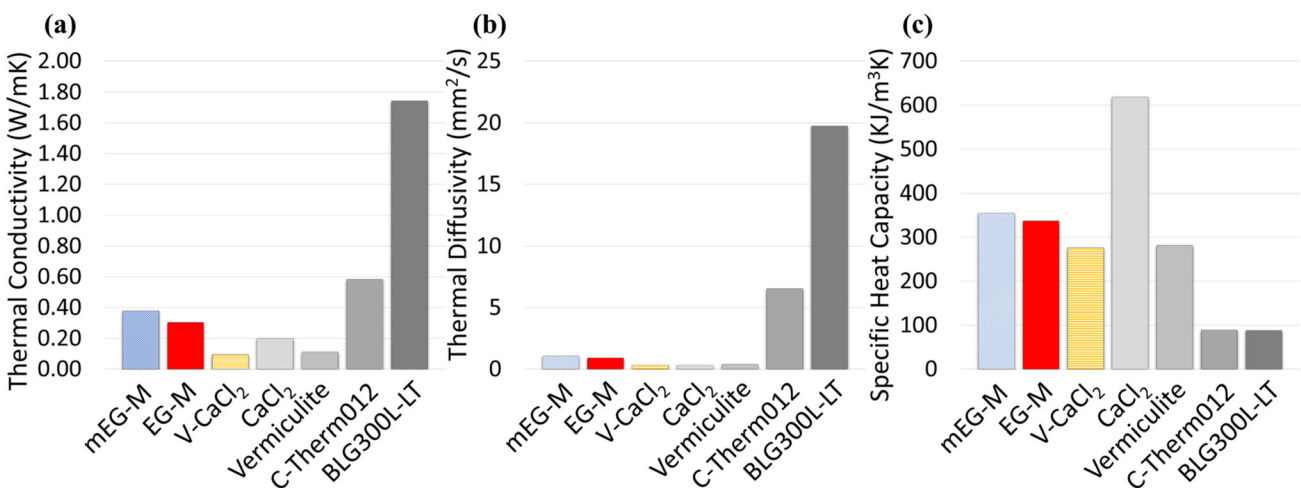


**Figure 13** Result from Hotdisk Thermal Analyser of powder samples. Thermal conductivity (a). Thermal diffusivity (b). Specific heat capacity (c).

C-Therm012 thermal conductivity value, whereas EG-M has only 17% of BLG300L-LT. Pure  $\text{CaCl}_2$  shows the largest specific heat value of all the materials and because this is the main component, specific heat of the composites will rely mainly on the  $\text{CaCl}_2$  content. As the salt content of the composites is increased, so does the specific heat capacity.

### Cyclability

To investigate the impact of cycling on output energy, several hydration/dehydration cycles were carried out for each material. Discharge conditions were kept constant at 25 °C, 60% RH, and 20 l/min for a period of 3 h. To ensure consistency between cycles, materials were removed from the reactor and placed in an oven at 120 °C for > 48 h. The study comprised of five cycles, and the energy discharged over a 3-h period is shown in Fig. 14.

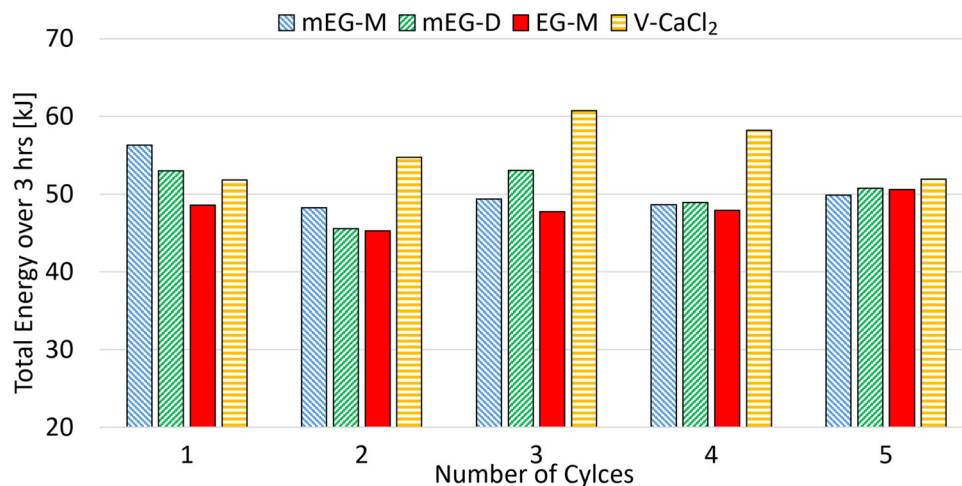
All the materials demonstrate a high level of reproducibility in their energy output. For the mEG-M sample, the total energy output drops by 8 kJ from cycle 1–2 but remains consistent within a range of 1.6 kJ between cycles 2–5. This indicates that the salt has migrated to a more stable position within the bead, which may have reduced reaction kinetics from that observed in cycle 1. The mEG-D and EG-M samples also show a drop in output energy after the first cycle, but no specific trend is observed thereafter. The mEG-D sample exhibits maximum energy output during cycle 3, whereas the EG-M sample has a maximum energy output during cycle 5. The range for mEG-D and EG-M is 7.5 kJ and 5.3 kJ, respectively. These results could be influenced by the

degree of particle fusion during charge cycles. Unlike the mEG-M sample, both the EG-M and mEG-D tend to form clusters of beads, and the extent of particle fusion would affect the reaction kinetics and, consequently, the output energy. The V- $\text{CaCl}_2$  sample displays an increase in energy output from cycle 1–3, followed by a decrease in each subsequent cycle, with the highest energy range of 8.9 kJ recorded. Since V- $\text{CaCl}_2$  is synthesised using the incipient wetness technique, the salt may take three cycles to migrate further into the particles, enhancing the contact area between the salt and the humid air. A subsequent decrease in energy output can be attributed to particle fusion and breakdown during cycle transfer.

### Conclusion

The successful synthesis of various EG/Alg based composites containing  $\text{CaCl}_2$  are presented. Size, shape, and material quantity can be easily changed using the described synthesis methods to suit the application. In this case, repeatable spherical beads of 6 mm diameter are produced using the mould method and beads ranging between 3 and 4 mm are produced using the drop-cast method. A higher salt encapsulation percentage (wt%) than previously studied V- $\text{CaCl}_2$  is achieved with both methods, reaching 84% in the mEG-M sample. An even distribution of salt is shown throughout the beads. Due to its spherical shape, it is possible to achieve high salt volumetric densities with a high packing density. This is crucial when considering these materials for transportation and domestic heat storage. Good air

**Figure 14** The heat energy produced from each material over five 3 h cycles of 60%RH and 25 °C at 20 l/min.



flow can also be expected in a packed bed reactor due to the spherical nature of the beads. This is indicated by the V-CaCl<sub>2</sub> creating a very moist bottom layer during discharge reactions in a packed bed whereas the larger beads (mEG-M and EG-M) do not. The output of heat energy is very promising for achieving results like that of V-CaCl<sub>2</sub> while having a far superior amount of un-released energy at the point where V-CaCl<sub>2</sub> is considered exhausted. The mEG-M demonstrates the most consistent discharge performance over multiple cycles, subsequent to the initial cycle. This stability is primarily due to the negligible particle fusion, breakdown, and material loss during cycles and transfer. As for the dehydration process, V-CaCl<sub>2</sub> performs better at small scale (5 g) which is a comparison in terms of mass. To further assess the charge performance, materials should be analysed at a larger scale in volumetric terms. Bead charge efficiency should improve as a result of the beads' superior air flow and salt volumetric densities. Charge reactions may only be possible on a larger scale with a heat exchanger, where the degree of heat transport will be crucial. The results of the thermal conductivity test show that expanded graphite composites will perform better than vermiculite-based composites. To further our knowledge on this, larger thermal analysis studies should be conducted on materials in their aggregate form. The fact that size and shape can be altered to enhance these outcomes is one advantage of utilising EG/Alg materials.

Owing to the straightforward and scalable synthesis routes, both methods of synthesis can be easily scaled up for use in a commercial setting. In addition, only materials that are inexpensive, abundant, and non-toxic are utilised. Larger-scale tests with sufficient cyclability as a significant objective should be carried out in order to advance this work forward towards actual heat storage. The ability of salt hydrates to deliquesce is a common issue. Material stability over time could be improved if this could be avoided or contained.

## Acknowledgements

The authors would like to thank the Materials and Manufacturing Academy and COATED CDT (COATED M2A) in Swansea University, TATA Steel Colors, Engineering and Physical Sciences Research Council (EPSRC via UKRI) EP/S02252X/1, and the

European Social Fund via the Welsh Government (WEFO) (c80816) for supporting the work described in this article. SEM/EDS were performed using the Advance Imaging of Materials (AIM) facilities at Swansea University, supported by the European Regional Development Fund through the Welsh Government (80708) & EPSRC (EP/M028267/1).

## Declarations

**Conflict of interest** The authors declare that they have no conflict of interest.

**Open Access** This article is licensed under a Creative Commons Attribution 4.0 International License, which permits use, sharing, adaptation, distribution and reproduction in any medium or format, as long as you give appropriate credit to the original author(s) and the source, provide a link to the Creative Commons licence, and indicate if changes were made. The images or other third party material in this article are included in the article's Creative Commons licence, unless indicated otherwise in a credit line to the material. If material is not included in the article's Creative Commons licence and your intended use is not permitted by statutory regulation or exceeds the permitted use, you will need to obtain permission directly from the copyright holder. To view a copy of this licence, visit <http://creativecommons.org/licenses/by/4.0/>.

## References

- [1] Ofgem (2016) Ofgem's future insights series: the decarbonisation of heat. [https://www.ofgem.gov.uk/system/files/docs/2016/11/ofgem\\_future\\_insights\\_programme\\_-\\_the\\_decarbonisation\\_of\\_heat.pdf](https://www.ofgem.gov.uk/system/files/docs/2016/11/ofgem_future_insights_programme_-_the_decarbonisation_of_heat.pdf). Accessed 1 Jul 2022
- [2] Ofgem (2020) Ofgem decarbonisation action plan. [https://www.ofgem.gov.uk/system/files/docs/2020/02/ofg1190\\_decarbonisation\\_action\\_plan\\_revised.pdf](https://www.ofgem.gov.uk/system/files/docs/2020/02/ofg1190_decarbonisation_action_plan_revised.pdf). Accessed 1 Jul 2022
- [3] Climate change act 2008 (2008) The target for 2050. <https://www.legislation.gov.uk/ukpga/2008/27/part/1/crossheading/the-target-for-2050>. Accessed 1 Jul 2022
- [4] Jarimi H, Aydin D, Yanan Z et al (2019) Review on the recent progress of thermochemical materials and processes for solar thermal energy storage and industrial waste heat recovery. *Int J Low Carbon Technol* 14:44–69
- [5] Krönauer A, Lävemann E, Brückner S, Hauer A (2015) Mobile sorption heat storage in industrial waste heat

- recovery. *Energy Proc* 73:272–280. <https://doi.org/10.1016/j.egypro.2015.07.688>
- [6] Krese G, Koželj R, Butala V, Stritih U (2018) Thermochemical seasonal solar energy storage for heating and cooling of buildings. *Energy Build.* 164:239–253. <https://doi.org/10.1016/j.enbuild.2017.12.057>
- [7] Casey SP, Elvins J, Riffat S, Robinson A (2014) Salt impregnated desiccant matrices for “open” thermochemical energy storage—selection, synthesis and characterisation of candidate materials. *Energy Build* 84:412–425. <https://doi.org/10.1016/j.enbuild.2014.08.028>
- [8] Mohapatra D, Nandanavanam J (2022) Salt in matrix for thermochemical energy storage—a review. *Mater Today Proc* 72:27–33. <https://doi.org/10.1016/j.matpr.2022.05.453>
- [9] Brancato V, Gordeeva LG, Capri A et al (2021) Experimental comparison of innovative composite sorbents for space heating and domestic hot water storage. *Curr Comput-Aided Drug Des* 11:476. <https://doi.org/10.3390/cryst11050476>
- [10] Sutton R, Jewell E, Searle J, Elvins J (2018) Discharge performance of blended salt in matrix materials for low enthalpy thermochemical storage. *Appl Therm Eng* 145:483–493. <https://doi.org/10.1016/j.applthermaleng.2018.09.052>
- [11] Casey SP, Aydin D, Elvins J, Riffat S (2017) Salt impregnated desiccant matrices for ‘open’ thermochemical energy conversion and storage—improving energy density utilisation through hydrodynamic & thermodynamic reactor design. *Energy Convers Manag* 142:426–440. <https://doi.org/10.1016/j.enconman.2017.03.066>
- [12] Courbon E, D’Ans P, Permyakova A et al (2017) A new composite sorbent based on SrBr<sub>2</sub> and silica gel for solar energy storage application with high energy storage density and stability. *Appl Energy* 190:1184–1194. <https://doi.org/10.1016/j.apenergy.2017.01.041>
- [13] Zhang YN, Wang RZ, Li TX (2018) Thermochemical characterizations of high-stable activated alumina/LiCl composites with multistage sorption process for thermal storage. *Energy* 156:240–249. <https://doi.org/10.1016/j.energy.2018.05.047>
- [14] Casey SP, Aydin D, Riffat S, Elvins J (2015) Salt impregnated desiccant matrices for “open” thermochemical energy storage—hydrothermal cyclic behaviour and energetic analysis by physical experimentation. *Energy Build* 92:128–139. <https://doi.org/10.1016/j.enbuild.2015.01.048>
- [15] Salviati S, Carosio F, Saracco G, Fina A (2019) Hydrated salt/graphite/polyelectrolyte organic-inorganic hybrids for efficient thermochemical storage. *Nanomaterials* 9:420. <https://doi.org/10.3390/nano9030420>
- [16] Clark R, Mehrabadi A, Farid M (2020) State of the art on salt hydrate thermochemical energy storage systems for use in building applications. *J Energy Storage* 27:101145. <https://doi.org/10.1016/j.est.2019.101145>
- [17] Gaeini M, Rouws AL, Salari JWO et al (2018) Characterization of microencapsulated and impregnated porous host materials based on calcium chloride for thermochemical energy storage. *Appl Energy* 212:1165–1177. <https://doi.org/10.1016/j.apenergy.2017.12.131>
- [18] Salviati S, Carosio F, Cantamessa F et al (2020) Ice-templated nanocellulose porous structure enhances thermochemical storage kinetics in hydrated salt/graphite composites. *Renew Energy* 160:698–706. <https://doi.org/10.1016/j.renene.2020.07.036>
- [19] Kallenberger PA, Fröba M (2018) Water harvesting from air with a hygroscopic salt in a hydrogel-derived matrix. *Commun Chem* 1:6–11. <https://doi.org/10.1038/s42004-018-0028-9>
- [20] Kallenberger PA, Posern K, Linnow K et al (2018) Alginate-derived salt/polymer composites for thermochemical heat storage. *Adv Sustain Syst* 2:1700160. <https://doi.org/10.102/adsu.201700160>
- [21] Walsh S, Reynolds J, Abbas B et al (2020) Assessing the dynamic performance of thermochemical storage materials. *Energies* 13:2202. <https://doi.org/10.3390/en13092202>
- [22] Miao Q, Zhang Y, Jia X et al (2021) MgSO<sub>4</sub>-expanded graphite composites for mass and heat transfer enhancement of thermochemical energy storage. *Sol Energy* 220:432–439. <https://doi.org/10.1016/j.solener.2021.03.008>
- [23] Barreneche C, Fernández AI, Cabeza LF, Cuypers R (2015) Thermophysical characterization and thermal cycling stability of two TCM: CaCl<sub>2</sub> and zeolite. *Appl Energy* 137:726–730. <https://doi.org/10.1016/j.apenergy.2014.09.025>
- [24] Morishige K, Tateishi N (2003) Adsorption hysteresis in ink-bottle pore. *J Chem Phys* 119:2301–2306. <https://doi.org/10.1063/1.1585014>
- [25] Rammelberg HU, Schmidt T, Ruck W (2012) Hydration and dehydration of salt hydrates and hydroxides for thermal energy storage—Kinetics and energy release. *Energy Proc* 30:362–369. <https://doi.org/10.1016/j.egypro.2012.11.043>

**Publisher’s Note** Springer Nature remains neutral with regard to jurisdictional claims in published maps and institutional affiliations.